Journal of Materials Science: Materials in Electronics (2019) 30:10128–10137
https://doi.org/10.1007/s10854-019-01348-3

Influence of $Ca_2Nb_2O_7$ on the structure and electric properties of $CaBi_2Nb_2O_9$-based piezoceramics

Wan Li[1] · Jing Yuan[1] · Rui Nie[1] · Jia Chen[1] · Qiang Chen[1] · Jianguo Zhu[1]

Received: 18 February 2019 / Accepted: 15 April 2019 / Published online: 22 April 2019

Abstract
A series of piezoelectric ceramics with the formula $(1-x)Ca_{0.92}(LiCe)_{0.04}Bi_2Nb_2O_9 + xCa_2Nb_2O_7$ (CBNLC–CNO-*x,* where $x = 0, 0.05, 0.1, 0.15, 0.2$) were prepared by a facile traditional solid-state reaction method. The phase structure, Raman spectra, microstructure, dielectric properties, electric properties, piezoelectric properties and thermal stabilities of the obtained CBNLC–CNO-*x* ceramics were studied. X-ray diffraction revealed that the obtained ceramics had a typical bismuth layer structure with secondary phases of $Ca_2Nb_2O_7$. The Rietveld refinement and Raman spectra revealed a lattice distortion in the CBNLC–CNO-*x* ceramics, which influenced the piezoelectric properties. Scanning electron microscopy indicated that the grain size of the ceramics gradually decreased with increasing *x* value. The Curie temperature (T_c) of the ceramics was retained at an elevated temperature of approximately 926–940 °C and was close to that of pure CBN. The obtained ceramics showed great thermal stabilities, relative densities, dielectric properties and piezoelectric properties, which are beneficial for high-temperature applications.

1 Introduction

Piezoelectric ceramics are important functional materials that can convert electrical signals to mechanical signals and vice versa [1]. They are widely used in commercial applications, including ultra sound transducers, sensors, ferroelectric random access memory, and optoelectronic applications [2–4].

In recent years, lead-free piezoelectric ceramics have received widespread attention because of their environmental friendliness [5]. Lead-free piezoelectric ceramics can be divided into the following three types of crystal structures: perovskite, tungsten bronze, and bismuth layer [6]. The lead-free piezoelectric ceramics with a perovskite structure that are currently studied mainly focus on barium titanate ($BaTiO_3$, BT)-based, sodium barium titanate ($Na_{0.5}Bi_{0.5}TiO_3$, BNT)-based and sodium potassium niobate ($K_{0.5}Na_{0.5}NbO_3$, KNN)-based ceramics [7–13]. Compounds with a tungsten bronze structure have a structure related to tetragonal potassium tungsten bronze, K_xWO_3 [14].

Compared with the other two types of lead-free ceramics, Aurivillius-type bismuth layer-structured ferroelectric (BLSF) ceramics have unique properties, such as a high Curie temperature (T_C), an excellent thermal stability and fatigue-free properties, which allow BLSF ceramics to be used in high-temperature applications [15]. However, the piezoelectricity of BLSF ceramics is low due to the two-dimensional orientation restriction for spontaneous polarization (P_s) and the high coercive fields (E_c) [16]. In addition, to avoid high-voltage breakdown in high-temperature applications, a high electrical resistivity is strictly required. A low electrical resistivity at high temperature gives rise to a charge drift that interferes with piezoelectrically induced charges, which limits the use of low-resistivity materials in high-temperature applications [17]. Therefore, it is vital to synthesize BLSF ceramics with excellent resistivity and piezoelectric properties.

The general formula for Aurivillius family compounds is $(Bi_2O_2)^{2+}(A_{m-1}B_mO_{3m+1})^{2-}$, where A is a mono-, di-, or trivalent ion or a mixture that occupies 12-coordination sites; B is a tri-, tetra-, penta-, or hexavalent ion suited for octahedral coordination; and *m* is the number of octahedral layers in the perovskite slab in the range of 1–6 [18, 19]. Calcium bismuth niobate ceramics, $CaBi_2Nb_2O_9$ (CBN), are Aurivillius-type materials with double octahedral layers that possess a high Curie temperature (T_c ~930 °C) [20], which

✉ Jianguo Zhu
nic0400@scu.edu.cn

[1] College of Materials Science and Engineering, Sichuan University, Chengdu 610064, China

makes them feasible for use in high-temperature devices. Generally, the d_{33} value of pure CBN ceramics is approximately 5 pC/N [21], and the resistivity is ~ 10^6 Ω cm at 500 °C and ~ 10^5 Ω cm at 600 °C [22, 23].

The perovskite-like layer structured (PLS) ferroelectrics with a formula of $A_nB_nO_{3n+2}$ ($n=2$–7) have an exceptionally high Curie temperature and very high electrical resistivity [24–26]. Their structure is characterized by corner-shared BO_6 octahedra and 12-coordinated A cations within the perovskite-like layers, which are linked by A cations at their boundaries [27]. $Ca_2Nb_2O_7$ (CNO) is a PLS $A_nB_nO_{3n+2}$-type compound with $n=4$ [28]. Single-crystal CNO has an extremely high Curie point ($T_c > 1500$ °C), and the resistivity of CNO is several orders of magnitude higher than that of CBN [29, 30].

Substantial effort has been made to improve the piezoelectric properties and electrical resistivity of BLSF ceramics. Most of these studies have been concentrated on modification of the ions or oxide and new preparation techniques [31–33]. Recently, some reports indicated that ceramic–ceramic (two-phase) composites could have enhanced properties, such as dielectric properties and magnetic properties [34–36]. Additionally, some reports have indicated that the introduction of a secondary phase into a ceramic matrix, such as Al_2O_3/ZrO_2, could be an effective way to improve the density and decrease ionic conductivity [17, 37].

To synthesize CBN-based high-temperature piezoelectric ceramics with excellent resistivity and piezoelectric properties, $Ca_2Nb_2O_7$ was added to modify the (Li, Ce)-substituted CBN ceramics. The results showed that the doping of Li and Ce could greatly improve the piezoelectric properties of the CBN [30, 38]. The addition of $Ca_2Nb_2O_7$ with a high electrical resistivity may enhance the resistivity of CBN-based ceramics. The mechanism involved in the improvement of the piezoelectric and electrical properties is discussed.

2 Experimental procedure

The $(1-x)Ca_{0.92}(LiCe)_{0.04}Bi_2Nb_2O_9 + xCa_2Nb_2O_7$ (CBNLC–CNO-x, $x=0$, 0.05, 0.1, 0.15, 0.2) ceramics were prepared by a solid-state two-step reaction route. Commercially available $CaCO_3$ (99%), Bi_2O_3 (99.999%), Nb_2O_5 (99.5%), Li_2CO_3 (99.99%), and CeO_2 (99.99%) were used as raw materials in the CBNLC ceramics. $CaCO_3$ (99%), Bi_2O_3 (99.999%), and Nb_2O_5 (99.5%) were used in the CNO ceramics. The raw materials were carefully weighed according to the stoichiometric compositions and subsequently ball mixed for 24 h. The obtained mixed powders of CBNLC were dried and calcined at 850 °C for 3 h. The mixed powders of CNO were dried and calcined at 1250 °C for 3 h. Then, the above two types of composite were mixed according to the required ratio, ball milled for 24 h and pressed into a pellet using polyvinyl alcohol (PVA) as a binder under a pressure of 10 MPa. The PVA binder was removed by heating the pellets at 450 °C. Finally, the pellets were sintered between 1150 and 1250 °C for 3 h to improve the crystallinity.

The phase composition of the obtained ceramics was detected by X-ray diffraction (XRD) employing Cu Kα radiation (EMPYREAN, PANalytical B.V., Netherlands). The scattering Raman spectra of all the ceramics were obtained with a Raman spectrometer at an excitation wavelength of 532 nm from an argon ion laser (LabRAM HR, HORIBA, France). The microstructure and element distribution of these ceramics was investigated by scanning electron microscopy (SEM, JSM-7500F, JEOL, Japan). The relative bulk density of the obtained ceramics was measured according to the Archimedes principle. The dielectric behaviour as a function of temperature was determined using a precision LCR analyzer (E4980A, Agilent, US) connected with a programmable furnace. The ceramics were poled at 180 °C in a silicon oil bath under a DC electric field of 9–10 kV/mm for 15 min. A quasi-static d_{33} m (ZJ-3A, Institute of Acoustics, Academia Sinca, China) was used to measure the piezoelectric coefficient d_{33}. The thermal depoling experiments were carried out by holding the poled samples for 2 h at every anneal temperature from room temperature to 940 °C, and the corresponding d_{33} value was measured at room temperature. The ferroelectric properties of the obtained products were determined using an aixACCT TF 2000 analyzer.

3 Results and discussion

X-ray diffraction is a useful technique to investigate the phase composition of composites. Figure 1 shows the XRD patterns of CBNLC–CNO-x ceramics scanned from 10° to 70°. The obtained XRD pattern of CBNLC–CNO-0 matched well with a typical Aurivillius phase in the standard powder diffraction card (JCPDS 49-0608). Among the diffraction planes, the highest intensity occurred for the (115) planes, which is consistent with the theory that the most intense diffraction peak of the Aurivillius phase is from a [11($2m+1$)] type of plane [22, 23]. Two additional diffraction peaks ($x>0$) appeared at approximately 48.8° and 58°, which can be indexed to $Bi_8Nb_{18}O_{57}$ (JCPDS 16-0325) and $CaNb_2O_7$ (JCPDS 74-0390), respectively. The diffraction intensity of these two peaks gradually increased as the x value increased, implying an increase in the content of the secondary phase.

To further analyse the influence of the $Ca_2Nb_2O_7$ doping on the obtained CBNLC–CNO-x ceramic crystal structure, a Rietveld refinement using Maud software was conducted, as shown in Fig. 2. The spectrum of CBNLC–CNO-0 is well matched with the calculated data of CBN space group

$A2_1am$, and no secondary phases can be found. With the introduction of CNO, the $Ca_2Nb_2O_7$ phase and $Bi_8Nb_{18}O_{57}$ phase can be detected in the ceramics. Refinement factors indicated that the content of the $Bi_8Nb_{18}O_{57}$ phase was very small compared with the $Ca_2Nb_2O_7$ phase. The fitted lattice parameters and phase composition of the CBNLC–CNO-x ceramics are shown in Fig. 3. A slight decreasing trend with increasing x value can be observed, implying a lattice distortion in the samples. It should be noted that the content of the CNO phase increased with increasing x value, and the designed phase composition is very close to the fitted phase composition. The results above demonstrated that the CNO secondary phase formed in the obtained CBNLC–CNO-x ($x > 0$) ceramics.

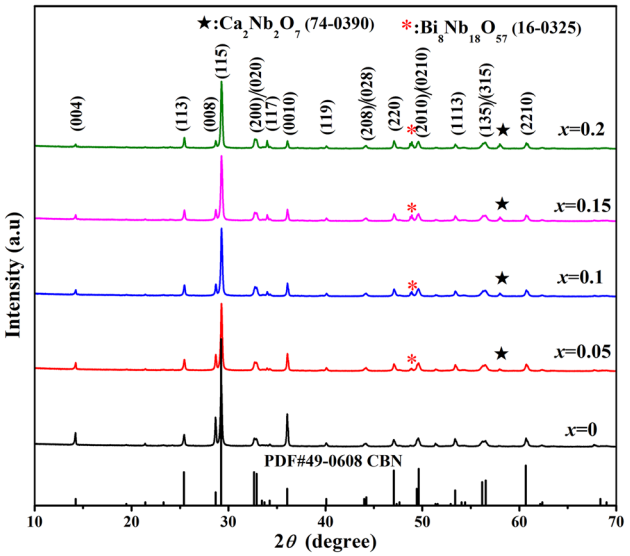

Fig. 1 XRD patterns of CBNLC–CNO-x ceramics

Raman spectroscopy was further carried out to investigate the vibration modes of the obtained CBNLC–CNO-x ceramics in the range of 100–1200 cm^{-1} at room temperature, as shown in Fig. 4. It should be noted that Raman phonon modes were mainly derived from the main Aurivillius phase, and it was difficult to detect a new mode from the secondary phase with a small content. Therefore, all samples exhibited similar phonon modes at approximately 185, 208, 277, 297, 324, 450, 590 and 822 cm^{-1}. For the Raman spectrum of the bismuth layer-structured crystals, the phonon modes can be

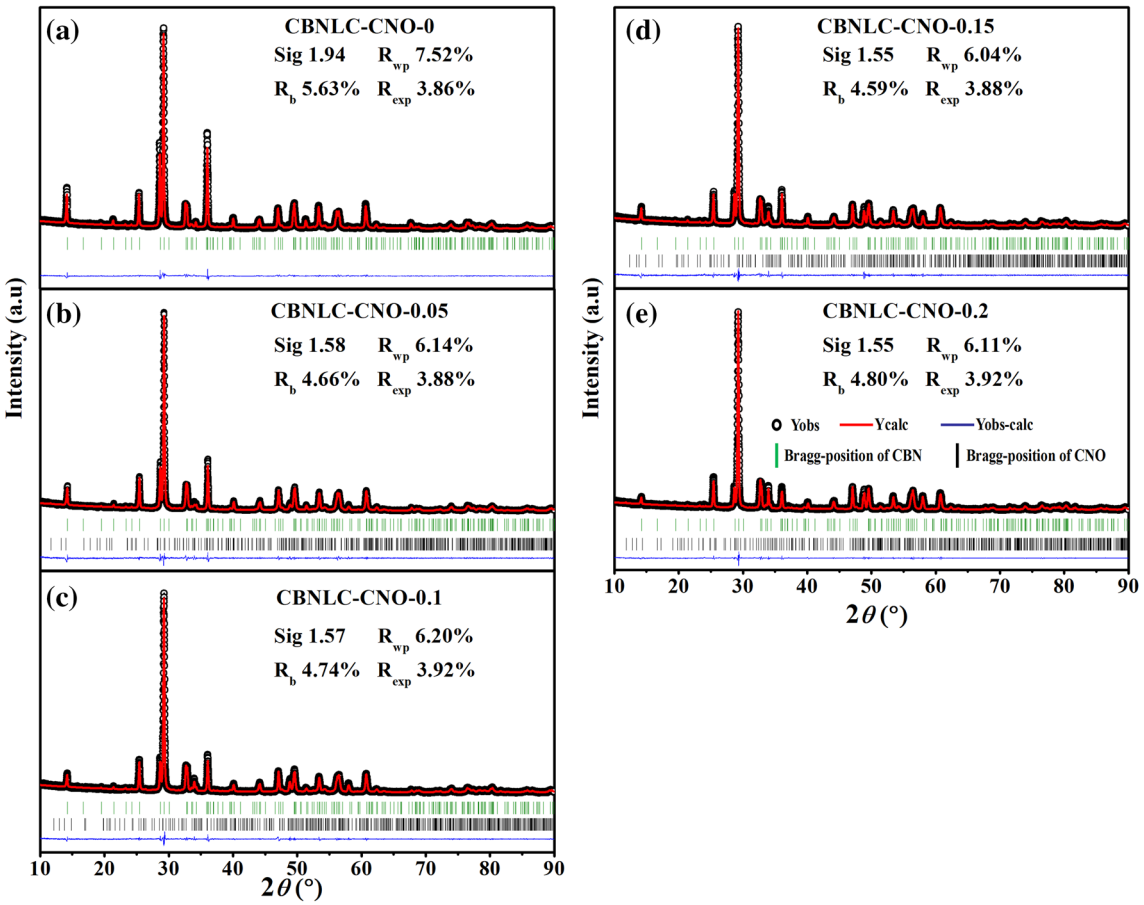

Fig. 2 Rietveld refinement on XRD patterns of CBNLC–CNO-x ceramics

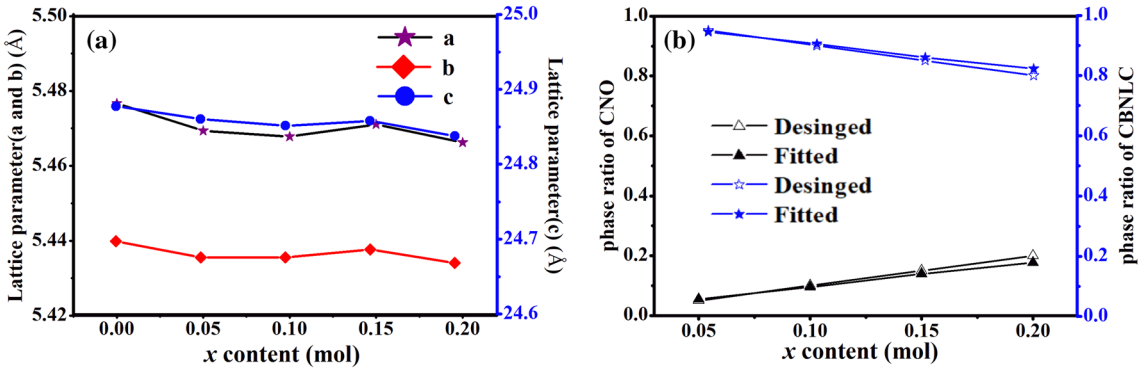

Fig. 3 **a** The fitted parameters and **b** phase composition of CBNLC–CNO-*x* ceramics

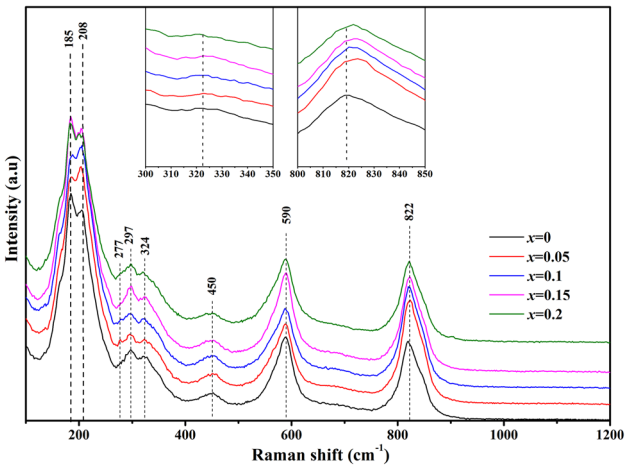

Fig. 4 The Raman spectra of CBNLC–CNO-*x* samples at room temperature

classified into two categories: low-frequency modes below 200 cm^{-1} and high-frequency modes above 200 cm^{-1} [39]. The low-frequency modes below 200 cm^{-1} are related to the cation vibration in the perovskite layers [32], and the modes at approximately 208 cm^{-1} are associated with the vibration of the A-site cations in the perovskite layers [38]. The high-frequency modes above 200 cm^{-1} primarily came from the torsional bending and the stretching modes of the BO_6 octahedra. The modes at approximately 450 cm^{-1} and 590 cm^{-1} were associated with the vibration of the top oxygen atom at the oxygen octahedron. The mode at 822 cm^{-1} was due to the symmetric stretching of the NbO_6 octahedron [40]. The mode at 822 cm^{-1} shifted to a higher frequency with increasing *x* content, which may suggest that the CNO substitution in CBNLC ceramics may occupy the B-site in the perovskite layers [41].

Figure 5 shows SEM micrographs of the natural surface of the CBNLC–CNO-*x* ceramics. All of the samples show a typical plate-like structure owing to the crystal growth anisotropy [30]. As *x* increased, the particle size of the samples gradually decreased. To further analyse the average grain size and relative density of CBNLC–CNO-*x* ceramics, the grain size was calculated through statistical methods by Nano Measurer software. The relative density of the samples was measured by the Archimedes method. Figure 6 displays the calculated average grain size and relative density of the ceramics. The grain size of the ceramics decreased with increasing *x* value, but the relative density shows the opposite trend.

To investigate the element distribution of the obtained products, energy dispersive spectrometry (EDS) was conducted on the CBNLC–CNO-0.2 sample. As shown in Fig. 7, the atomic percentage of Ca was higher in the grain boundaries (as implied by the enrichment of the coloured pixel points and spectrums) than in the grains. This means that Ca is enriched near the CBN grain boundaries. The atomic percentage of Ca in CNO is higher than CBN. From this, we can infer that the secondary phase was enriched near the CBN grain boundaries as the *x* value increased for the CBNLC–CNO-*x* ceramics, which could hinder the growth of the grains during the calcination process [42]. Thus, small grains can be observed in the SEM results. It can be assumed that pores and voids can be easily generated at the triple grain junctions within the bulk ceramics if the plate-like grains randomly stack. These pores and voids are undesirable for electrical resistivity upon densification because they may form electric current paths [17]. The smaller size and aspect ratio of grains reduced pores and voids in ceramics, resulting in an improvement in the relative density of ceramics [17]. It can be concluded that CNO addition could improve the density and may further improve the resistivity of CBNLC ceramics in this case.

Figure 8a displays the complex impedance plots of obtained CBNLB-CNO-*x* ceramics measured at 500 °C. The complex impedance can be represented by a sequence of equivalent circuits consisting of a resistance and constant phase element [43]. It can be inferred from Fig. 8a that only

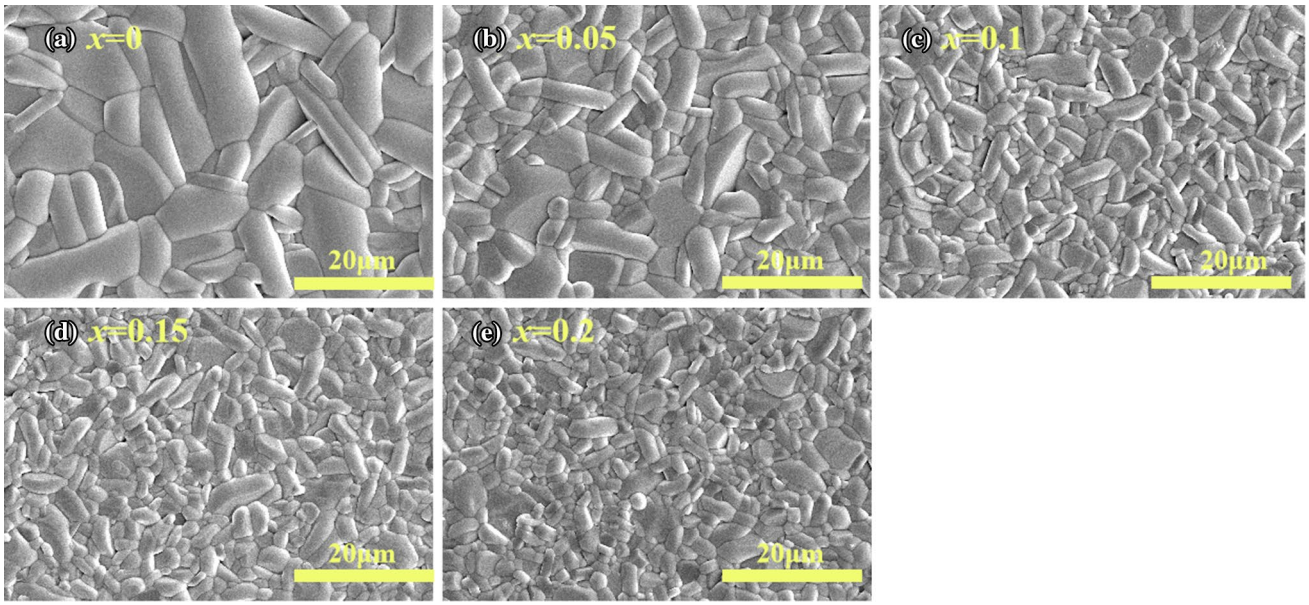

Fig. 5 **a**–**e** SEM micrographs of CBNLC–CNO-*x* ceramics

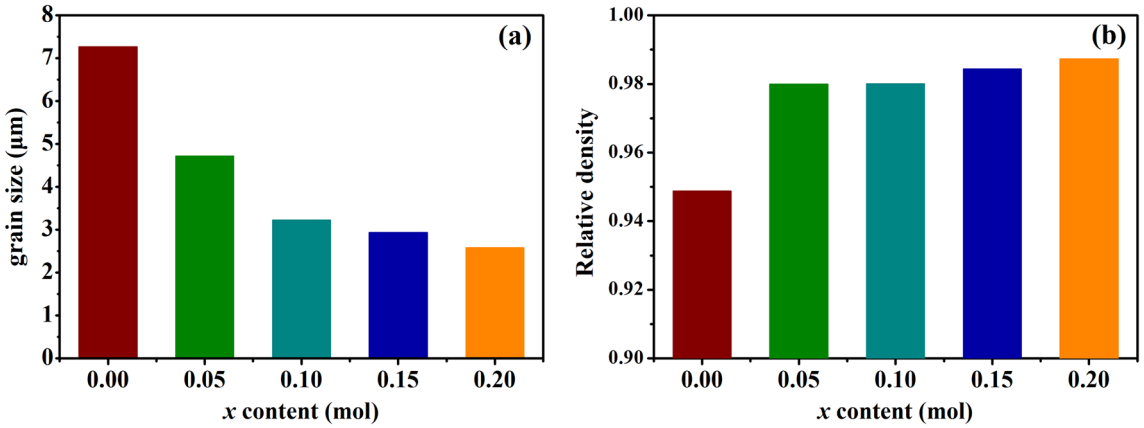

Fig. 6 **a** Average grain size statistical distribution map and **b** relative density of CBNLC–CNO-*x* ceramics

one semicircle can be observed in the Nyquist plots for all samples, suggesting a dominant behaviour of the grains [31]. The diameter of the semicircles increased with increasing *x* value, indicating an increase in the resistance of the obtained products. Figure 8b illustrates that the *ac* conductivity (σ_{ac}) of CBNLC–CNO-*x* ceramics slightly increased with increasing frequency. The σ_{ac} decreased with increasing *x* value at a constant frequency. This can be explained as follows. The frequency-dependent *ac* conductivity can be described by Jonscher's power law [44]:

$$\sigma_{ac} = \sigma_{dc} + A\omega^{n} \quad (1)$$

where σ_{ac} is the frequency-dependent alternate current conductivity, σ_{dc} is the frequency-independent direct current conductivity, and the coefficient A and exponent n ($0 < n < 1$) are constants related to the temperature and material intrinsic property, respectively. It should be noted that the frequency-dependent *ac* conductivity obeys the universal power law.

Figure 9 shows the fitted temperature-dependent dc resistivity obtained by formula (1) measured in the temperature range of 200–700 °C. With increasing temperature, the resistivity exponentially decreased. Figure 9b demonstrates that the resistivity of CBNLC–CNO-0.2 increased nearly one order of magnitude compared with that of the CBNLC–CNO-0 at 500 °C and 600 °C. The highly insulating secondary phase and the small grain size were formed with the addition of CNO, which can reduce the pores and voids and thus improve the density of the ceramics. It can

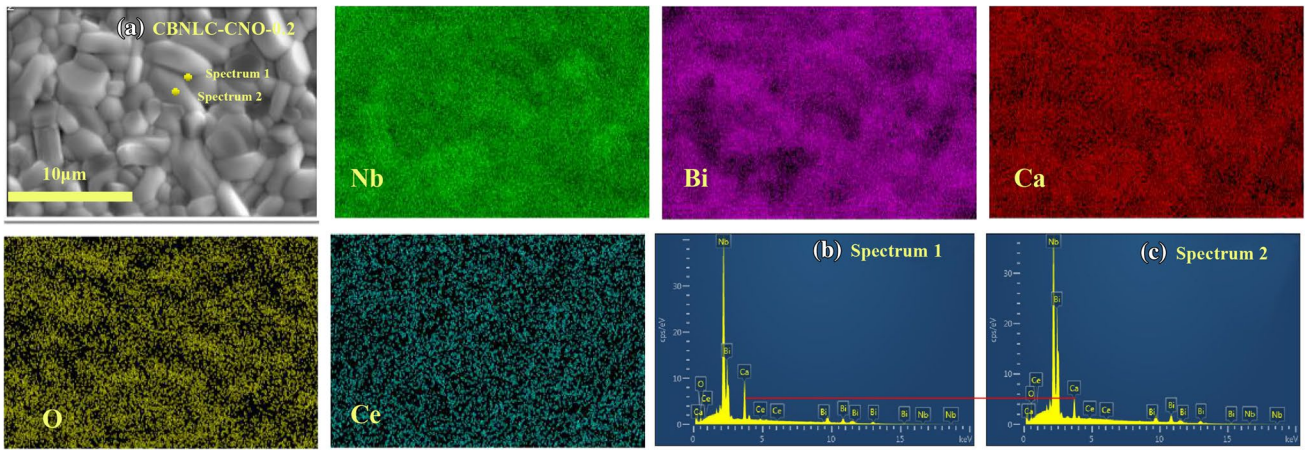

Fig. 7 Element distribution of CBNLC–CNO-0.2 ceramic and EDS analysis of **b** representative grain boundary (spectrum 1), **c** representative grain (spectrum 2)

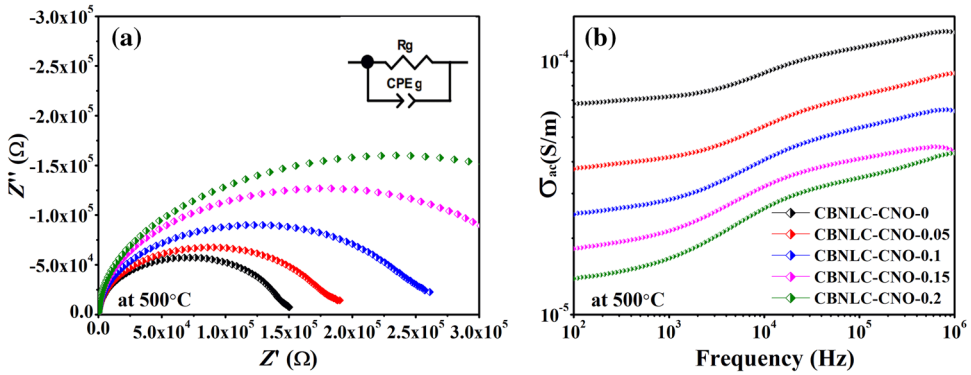

Fig. 8 **a** Complex impedance plots and **b** the corresponding frequency dependence of *ac* conductivity measured at 500 °C for CBNLC–CNO-*x* ceramics

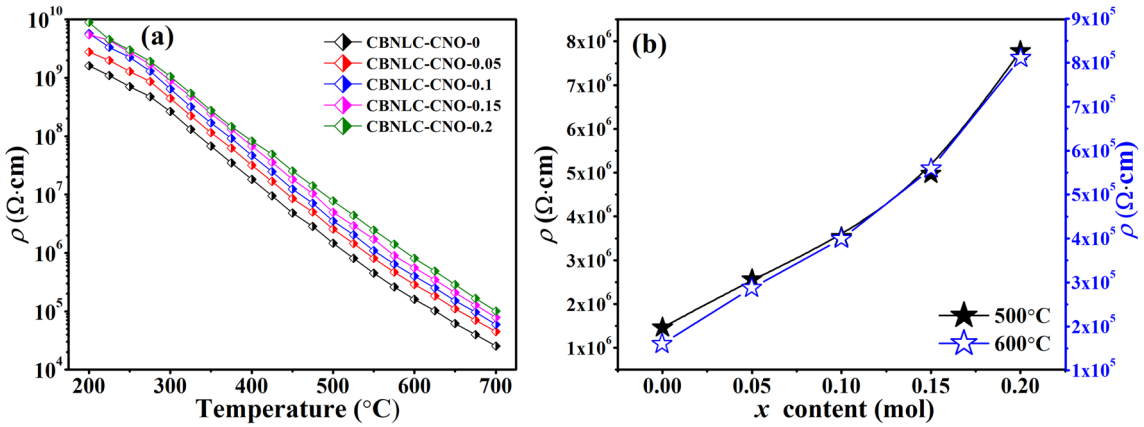

Fig. 9 Resistivity of CBNLC–CNO-*x* ceramics as a function of measuring temperature

be assumed that the addition of a secondary phase would result in a significant blocking effect on the electric current paths through grain boundaries and hence enhance the electrical resistivity [17].

Figure 10 shows the dielectric constant and dielectric loss of the CBNLC–CNO-*x* ceramics as a function of temperature. The Curie temperature of the CBNLC–CNO-*x* ceramics decreased from 942 to 926 °C with increasing *x* content. It

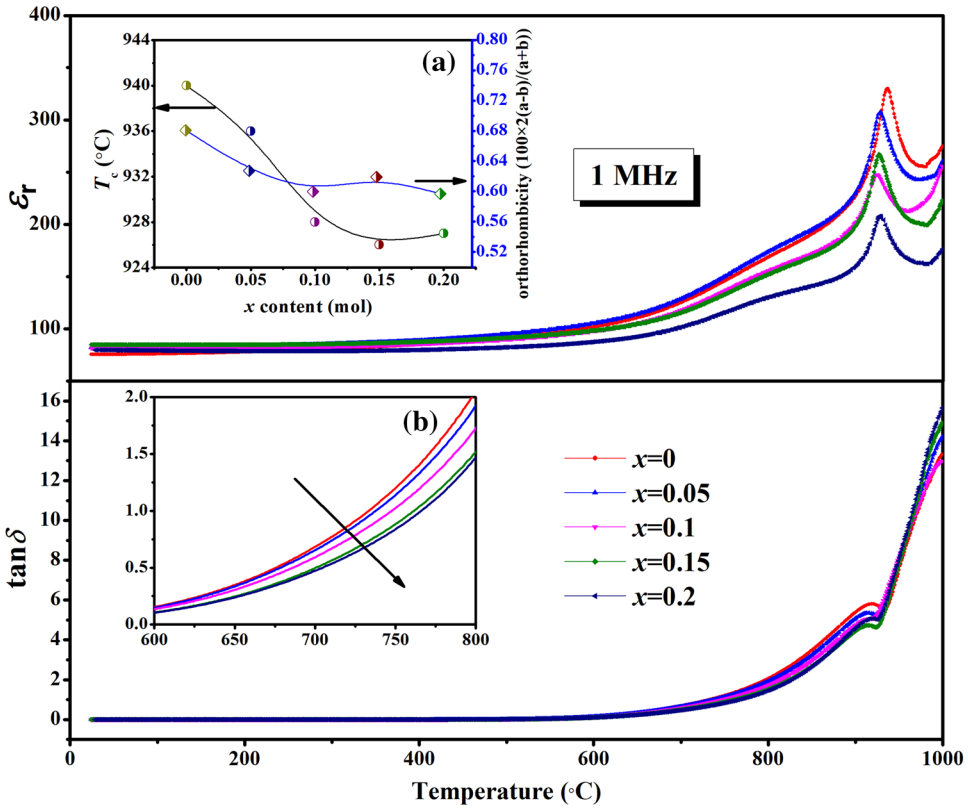

Fig. 10 Temperature dependence of the relative permittivity and the dielectric loss of the CBNLC–CNO-*x* ceramics measured at 1 MHz

should be noted that lattice distortion can strongly influence the Curie temperature T_C of Aurivillius-type compounds [43, 45]. As can be inferred from the Rietveld refinements and Raman spectra, the lattice distortion in the obtained ceramics was confirmed. To evaluate the degree of lattice distortion in the pseudo-perovskite structure of BLSF ceramics, orthorhombicity was introduced and defined as $2|(a-b)|/(a+b)$, where a and b are the lattice parameters [46]. Figure 10a displays the correlation between orthorhombicity and T_C value, both of which exhibit the same variation trend. The decrease in T_C was associated with a decrease in orthorhombicity [46].

Moreover, the dielectric loss values were found to be very low below 700 °C (< 1.2%). This phenomenon indicated that the CBNLC–CNO-*x* ceramics possessed stable dielectric properties in a rather large temperature range, which is beneficial for use in high-temperature applications. On the other hand, the dielectric loss of the CBNLC–CNO-*x* ceramics gradually decreased with the increasing amount of CNO addition. It can be assumed that the introduction of a secondary phase increased the density and resistivity of the obtained ceramics and then reduced the consumption of electrical energy under alternating electric fields, resulting in a reduction in the dielectric loss. The frequency-dependent *ac* conductivity is also given by [47]:

$$\sigma_{ac} = \omega C \tan\ \delta(d/S) \tag{2}$$

where C is the measured capacitance, ω is the angular frequency ($\omega = 2\pi f$), d is the thickness of sample, S is the area of sample, and tan δ is the dielectric loss.

Figure 11a and b shows the temperature-dependent *ac* conductivity of the CBNLC–CNO-0, CBNLC–CNO-0.1, and CBNLC–CNO-0.2 ceramics at 1 kHz, 10 kHz and 100 kHz. The *ac* conductivity of the ceramic increased with increasing frequency. The change rate of the σ_{ac} with temperature can be classified into two categories: the low-temperature range and high-temperature range.

The *ac* conductivity can be expressed as the Arrhenius equation [47]:

$$\sigma_{ac} = \sigma_0 \exp\left[-E_a/k_B T\right] \tag{3}$$

where σ_0 is a pre-exponential factor related to material characteristics, E_a is the activation energy for conduction, k_B is the Boltzmann constant, and T is the temperature in Kelvin, respectively. The calculated activation energy measured at 100 kHz for the CBNLC–CNO-0.2 ceramic was 1.31 eV for the high-temperature range and 0.04 eV for the low-temperature range. The similar results were observed in the CBNLC–CNO-0 and CBNLC–CNO-0.1 ceramics. This result implied that the different conduction mechanisms can be activated at different temperature ranges in the obtained samples. At low temperatures, E_a was close to the primary ionization activation energy of oxygen vacancies, which indicated that oxygen vacancy conductance dominated in

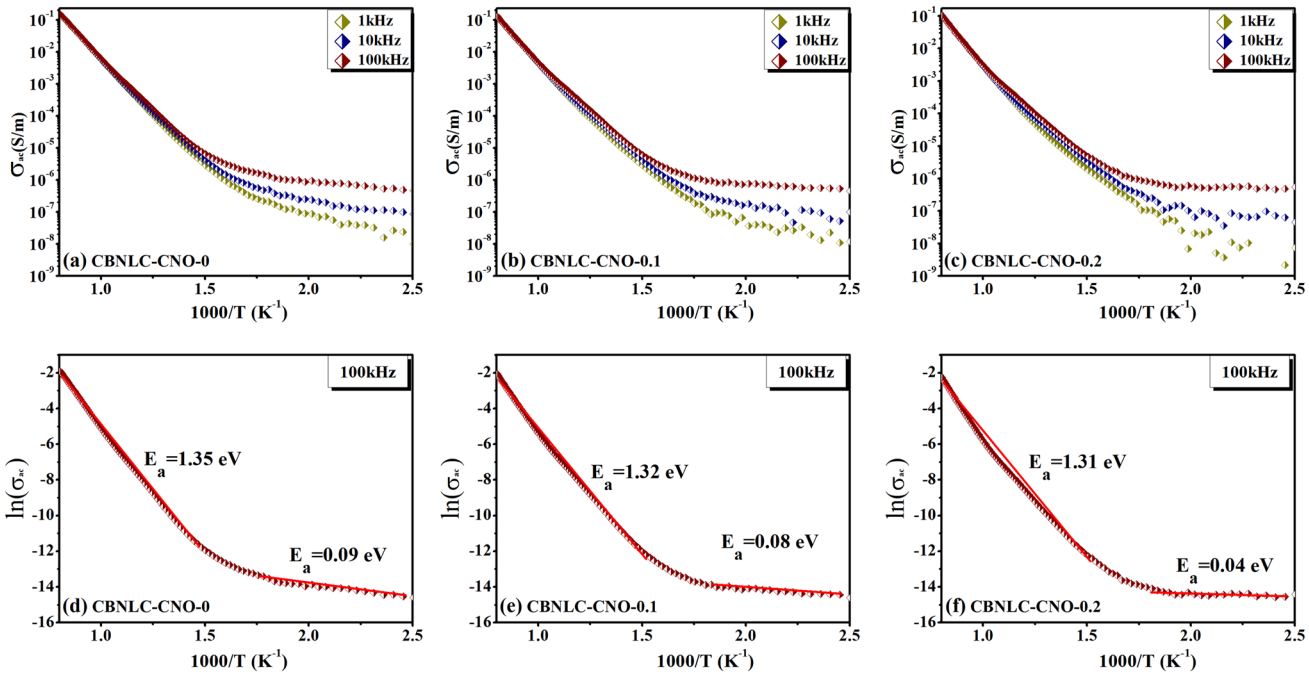

Fig. 11 The temperature dependent *ac* conductivity of CBNLC–CNO-0,CBNLC–CNO-0.1 and CBNLC–CNO-0.2 ceramics measured at 1 kHz, 10 kHz and 100 kHz

the low-temperature range. It is known that the intrinsic activation energy of intrinsic conduction is equal to half of the band gap energy (3.3 eV). In our measurement, the E_a values of obtained ceramics at high temperature (1.35 eV, 1.32 eV, and 1.31 eV) were close to this value (1.65 eV) [48]. This approximation indicated that the primary conduction mechanism in the ceramics changed to intrinsic conduction decided by the structure of the ceramic matrix at high temperatures. Moreover, the gradient in the *ac* conduction tended to be shallow with the increase in frequency at low temperature, which is suitable for application in high-frequency conditions.

Figure 13a shows values of the piezoelectric constant d_{33} versus x contents of the obtained CBNLC–CNO-x ceramics at room temperature. The piezoelectric constant was 16 pC/N (CBNLC–CNO-0) and decreased to 6.3 pC/N (CBNLC–CNO-0.2) with increasing x content, from which a linear relationship of d_{33} and CNO doping can be derived. Moreover, the piezoelectric performance was substantially affected by the lattice distortion in the Aurivillius phase [46]. As discussed in the Rietveld refinement and Raman results, the doping of CNO depressed the lattice distortion of the CBN, reducing the d_{33} value. In addition, the decrease in the grain size also contributed to the decrease in the d_{33} value [33, 49].

The polarization–electric (P–E) loops of the obtained CBNLC–CNO-x ceramics are shown in Fig. 12. It can be observed that samples with higher CNO contents possessed a higher coercive field (E_c), and it can be assumed that small grain sizes possessed the elevated internal stresses that were responsible for this phenomenon and gave additional resistance to the ferroelectric switch [49–51]. A sample with a small grain size has an increased number of grain boundaries. The strong coupling between the domain walls and grain boundaries makes the domain reorientation difficult and thus constrains the motion of the domain wall. The value of remnant polarization (P_r) is reduced because of the reduction in the achievable domain alignment. Moreover, the decrease in domain wall mobility of the ceramics also leads to a reduction in the piezoelectric coefficients [50, 51]. On the other hand, the second phase in the ceramics also has a decreased ferroelectricity, which contributes less to the piezoelectricity and consequently the value of d_{33} decreases.

Figure 13b displays the thermal depoling behaviour of the CBNLC–CNO-x ceramics. From the figure, we can observe that the variation of the piezoelectric constant can be divided into three stages. In the first stage, the piezoelectric constant of all samples reduced slightly between 200 and 500 °C due to the thermally activated reverse switching of the non-180° domain [52]. In the second stage from 500 to 900 °C, the d_{33} values of all samples remained unchanged. In the final stage, when the temperature reached 900 °C and above (close to the T_c), the d_{33} values of all samples decreased rapidly. In summary, the obtained CBNLC–CNO-x ceramics had excellent thermal stability, which is promising for high-temperature applications.

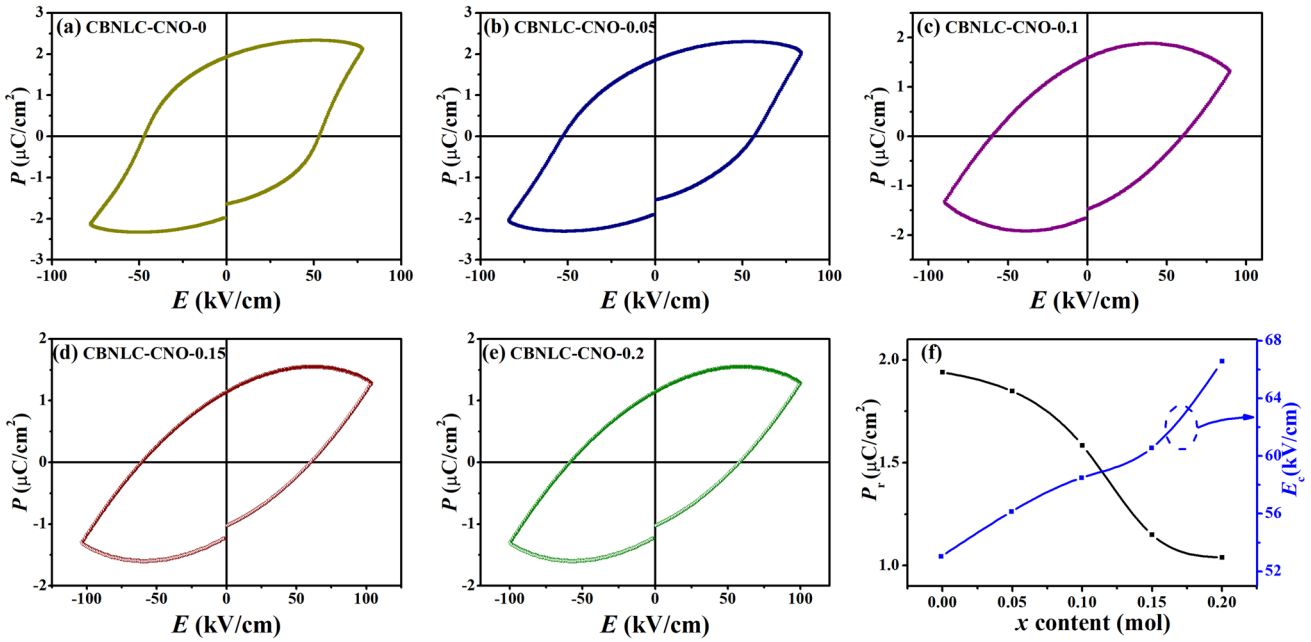

Fig. 12 *P–E* loops of CBNLC–CNO-*x* ceramics measured at 180 °C and 1 Hz

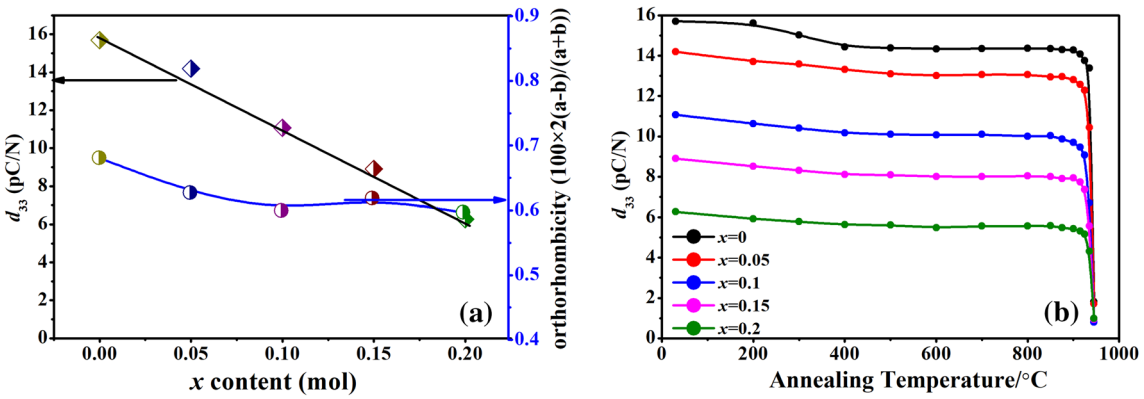

Fig. 13 **a** The piezoelectric constant d_{33} values at room temperature and **b** thermal depoling behaviour of CBNLC–CNO-*x* ceramics

4 Conclusions

$Ca_2Nb_2O_7$ doped CBNLC ceramics were synthesized by a facile two-step solid-state reaction route. X-ray and Rietveld refinement results showed that the doped ceramics changed from a typical bismuth layer structure to a bismuth layer structure with a PLS monoclinic phase. The SEM images showed that the average grain size of these ceramics decreased because of the doping effect. The Curie temperature of all samples remained at a high level that is above 925 °C. It was concluded that the formation of small grains and second phases reduced the pores and voids in the ceramics, improving the relative density, and caused significant blockage of the current path through the grain boundaries. An enhanced density, improved dc resistivity, and lower dielectric losses could observe in the modified ceramics. A compromise between T_c, polarizability, dielectric losses and electrical resistivity was achieved by the suitable addition of CNO. This work suggested that the introduction of $Ca_2Nb_2O_7$ is beneficial for (Li, Ce)-substituted CBN ceramics for high-temperature applications.

Acknowledgement This work was supported by National Natural Science Foundation of China (Grant No. 51332003) and Sichuan Science and Technology Program (Grant No. 2018G20140).

References

1. G.H. Haertling, J. Am. Ceram. Soc. **82**, 797 (1998)
2. P.K. Roy, B. Ponraj, K.B.R. Varma, Ceram. Int. **43**, 15762 (2017)
3. K. Praveena, K.B.R. Varma, J. Mater. Sci.: Mater. Electron. **25**, 3103 (2014)
4. S.P.P. Sadhu, P.W. Jaschin, S. Perumbilavil, A.R. Thomas, V.S. Muthukumar, R. Philip, K.B.R. Varma, Appl. Phys. B **124**, 200 (2018)
5. T.R. Shrout, S.J. Zhang, J. Electroceram. **19**, 113 (2007)
6. D.Q. Xiao, J.G. Wu, L. Wu, J.G. Zhu, P. Yu, D.M. Lin, Y.M. Liao, Y. Sum, J. Mater. Sci. **44**, 5408 (2009)
7. G. Arlt, D. Hennings, G. Dewith, J. Appl. Phys. **58**, 1619 (1985)
8. P.K. Panda, J. Mater. Sci. **44**, 5049 (2009)
9. L. Egerton, D.M. Dillon, J. Am. Ceram. Soc. **42**, 438 (1959)
10. P. Bharathi, P. Thomas, K.B.R. Varma, J. Mater. Chem. C. **3**, 4762 (2015)
11. R.K. Prusty, P. Kuruva, U. Ramamurty, T. Thomas, Solid State Commun. **173**, 38 (2013)
12. P. Kuruva, U.M.S. Rajaputra, S. Sanyadanam, R.M. Sarabu, Turk. J. Phys. **37**, 312 (2013)
13. J.F. Li, K. Wang, F.Y. Zhu, L.Q. Cheng, F.Z. Yao, J. Am. Ceram. Soc. **96**, 3677 (2013)
14. P.B. Jamieson, S.C. Abrahams, J.L. Bernstein, J. Chem. Phys. **48**, 5048 (1968)
15. S. Zhang, F. Yu, J. Am. Ceram. Soc. **94**, 3153 (2011)
16. C.M. Wang, L. Zhao, J.F. Wang, L.M. Zheng, J. Du, M.L. Zhao, C.L. Wang, Mater. Sci. Eng., B **163**, 179 (2009)
17. Z. Zhou, R. Liang, Y. Li, X. Dong, J. Am. Ceram. Soc. **98**, 3925 (2015)
18. E.C. Subbarao, J. Phys. Chem. Solids **23**, 665 (1962)
19. E.C. Subbarao, J. Am. Ceram. Soc. **45**, 166 (2010)
20. H. Chen, F. Fu, J.W. Zhai, Jpn. J. Appl. Phys. **50**, 050207 (2011)
21. H. Yan, H. Zhang, R. Ubic, M.J. Reece, J. Liu, Z. Shen, Z. Zhang, Adv. Mater. **17**, 1261 (2005)
22. C.M. Wang, S. Zhang, J.F. Wang, M.L. Zhao, C.L. Wang, Mater. Chem. Phys. **118**, 21 (2009)
23. X. Zhang, H. Yan, M.J. Reece, J. Am. Ceram. Soc. **91**, 2928 (2008)
24. J.K. Yamamoto, A.S. Bhalla, J. Appl. Phys. **70**, 4469 (1991)
25. S. Nanamatsu, M. Kimura, T. Kawamura, J. Phys. Soc. Jpn. **38**, 817 (1975)
26. F. Lichtenberg, A. Herrnberger, K. Wiedenmann, Prog. Solid State Chem. **36**, 253 (2008)
27. S. Nanamatsu, M. Kimura, J. Phys. Soc. Jpn. **36**, 1495 (2007)
28. H. Ning, H. Yan, M.J. Reece, J. Am. Ceram. Soc. **93**, 1409 (2010)
29. J. Chen, J. Yuan, S. Bao, Y. Wu, G. Liu, Q. Chen, D. Xiao, J. Zhu, Ceram. Int. **43**, 5002 (2017)
30. X.X. Tian, S.B. Qu, H.L. Du, L. Ye, Z. Xu, Chin. Phys. B **21**, 037701 (2012)
31. G. Liu, J. Yuan, R. Nie, L. Jiang, Z. Tan, J. Zhu, Q. Chen, J. Alloys Compd. **697**, 380 (2017)
32. S. Kumar, S. Kundu, D.A. Ochoa, J.E. Garcia, K.B.R. Varma, Mater. Chem. Phys. **136**, 680 (2012)
33. H. Chen, B. Shen, J. Xu, L. Kong, J.W. Zhai, J. Am. Ceram. Soc. **95**, 3514 (2012)
34. A. Srinivas, D.W. Kim, K.S. Honga, Appl. Phys. Lett. **83**, 1602 (2003)
35. K. Praveena, K.B.R. Varma, J. Mater. Sci.: Mater. Electron. **25**, 5403 (2014)
36. K. Praveena, K.B.R. Varma, J. Mater. Sci.: Mater. Electron. **25**, 111 (2014)
37. J.P. Angle, J.J. Steppan, P.M. Thompson, M.L. Mecartney, J. Eur. Ceram. Soc. **34**, 4327 (2014)
38. Y. Wang, J. Wu, Z. Peng, Q. Chen, D. Xin, D. Xiao, J. Zhu, Appl. Phys. A **119**, 337 (2015)
39. Q. Wang, H. Fan, C. Long, L. Huang, J. Mater. Sci. Mater. Electron. **25**, 2961 (2014)
40. J. Yuan, R. Nie, Q. Chen, J. Xing, J. Zhu, J. Alloys Compd. **785**, 475 (2019)
41. H. Hao, H. Liu, S. Ouyang, J. Electroceram. **22**, 357 (2009)
42. S. Tekeli, M. Guru, Ceram. Int. **34**, 137 (2008)
43. M. Takahashi, Y. Noguchi, M. Miyayama, Jpn. J. Appl. Phys. **41**, 7053 (2002)
44. A.K. Jonscher, Nature **267**, 673 (1977)
45. T. Jardiel, A. Caballero, M. Villegas, J. Am. Ceram. Soc. **116**, 511 (2008)
46. Z. Peng, D. Yan, Q. Chen, D. Xin, D. Liu, D. Xiao, J. Zhu, Curr. Appl. Phys. **14**, 1861 (2014)
47. A. Singh, S.K. Barik, R. Choudhary, P.K. Mahapatra, J. Alloys Compd. **479**, 39 (2009)
48. Z. Peng, X. Zeng, X. Yang, F. Cao, J. Zhu, Ceram. Int. **43**, 1249 (2017)
49. H. Zhang, H. Yan, H. Ning, M.J. Reece, M. Eriksson, Z. Shen, Y. Kan, P. Wang, Nanotechnology **20**, 385708 (2009)
50. M. Frey, Z. Xu, P. Han, D.A. Payne, Ferroelectrics **206**, 337 (1998)
51. M. Frey, D.A. Payne, Phys. Rev. B **54**, 3158 (1996)
52. H. Yan, H. Zhang, M.J. Reece, X.L. Dong, Appl. Phys. Lett. **87**, 082911 (2005)